A Novel Compressive Sensing-Based Multichannel HRWS SAR Imaging Technique for Moving Targets

Shaojie Li [ID], Shaohui Mei [ID], *Senior Member, IEEE*, Shuangxi Zhang [ID], *Member, IEEE*, Shuai Wan [ID], *Member, IEEE*, and Tao Jia [ID]

Abstract—When high-resolution wide-swath (HRWS) multichannel synthetic aperture radar (MC-SAR) system is used for ocean observation, vast amount of redundant data is generated, significantly limiting its applications. Though compressive sensing (CS)-based method has been applied to the traditional single-channel or dual-channel SAR imaging system, it is no longer applicable for MC-SAR due to the existence of channel error when using the space-time equivalent sampling technique for azimuth signal reconstruction. By analyzing such periodic channel error, i.e., frequency-dependence phase mismatch (FD-PM), in this article, a novel dictionary is constructed for CS-based HRWS MC-SAR imaging after an improved range cell migration correction method is applied. As a result, a novel CS imaging mode is proposed for the ocean moving target based on the sparsity of the target scattering centers, by which the amount of data in MC-SAR can be reduced by sampling below the Nyquist sampling rate and the swath width can be further increased. Experimental results show that the proposed method clearly eliminates the azimuth defocus and blur caused by low sampling rate and FD-PM, and significantly reduces the amount of data to about one-third when compared to sampling at the Nyquist rate.

Index Terms—Compressive sensing (CS), frequency-dependence phase mismatch (FD-PM), high-resolution wide-swath (HRWS), multichannel synthetic aperture radar (MC-SAR), sparse representation.

I. Introduction

AS AN active observation system, synthetic aperture radar (SAR) has been widely used in marine observation, crop growth observation, environmental detection, and other fields [1]–[4]. However, wide-swath and high azimuth resolution are always a contradiction in the traditional SAR system. The pulse repetition frequency (PRF) of radar transmitter generally needs to be low enough to achieve a wide swath, which may result in an azimuth ambiguity. In order to solve such problem, multiple receive apertures in azimuth have been proposed [5]–[7]. Such multichannel SAR (MC-SAR) enables high-resolution wide-swath (HRWS) imaging, in which range ambiguity can be suppressed by transmitting chirp signals and all channels receive echoes simultaneously [8]. However, limited by the Nyquist sampling rate, a large amount of data is generated in such an HRWS SAR imaging system, resulting in a very heavy burden over data storage and transmission. In many SAR imaging applications, such as SAR-based ocean observation, the targets of interest are often sparsely present. Consequently, a great majority of the observed data is unnecessary even for HRWS SAR imaging. Therefore, it is of great urgent to improve MC-SAR imaging algorithms to achieve higher azimuthal resolution with considerably low amount of data.

Compressive sensing (CS) theory, in which sparse signals can be sampled at a frequency below Nyquist rate to reconstruct with high accuracy by solving an optimization problem [9]–[12], has been widely applied to lots of data acquisition systems to reduce the amount of data to be recorded. In HRWS SAR imaging over ocean areas, compared with large observation scene, moving targets can be considered to be of just a small number of strong scattering points that contribute most of the energy of SAR images. Such strong sparse presentation property of moving targets in HRWS SAR imaging makes it possible to adopt CS theory to alleviate the burden of large data volumes. At present, CS theory has been successfully applied to radar signal processing or single-channel/dual-channel SAR imaging system [13]–[23]. For example, Zhang *et al.* proposed an improved CS-based high-resolution imaging algorithm [13], which was applied to short coherent processing interval to improve the performance of CS-based ISAR imaging in the case of strong noise by solving the l_1 minimization optimization. A CS-based ground moving target indication method was also proposed by sparsely sampling dual-channel SAR data in the azimuth direction [14]. However, in these existing CS-based SAR imaging techniques, the number of pulses and observation channels is generally limited. Moreover, the range cell migration (RCM), which is caused by target motion and radar platform motion during echo signal processing, has not been encountered in these CS-based SAR imaging, resulting in a reduction of imaging resolution.

Shaojie Li, Shaohui Mei, and Shuai Wan are with the School of Electronics and Information, Northwestern Polytechnical University, Xi'an 710129, China (e-mail: shaojie_lee52@mail.nwpu.edu.cn; meish@nwpu.edu.cn; swan@nwpu.edu.cn).

Shuangxi Zhang is with the School of Electronics and Information, Northwestern Polytechnical University, Xi'an 710129, China, and also with the Toll Microelectronic, Xi'an 710075, China (e-mail: shuangxizhang1984@163.com).

Tao Jia is with the Department of Electronic Engineering, Air Force Engineering University, Xinyang 464000, China (e-mail: Jiatao_AFEU@126.com).
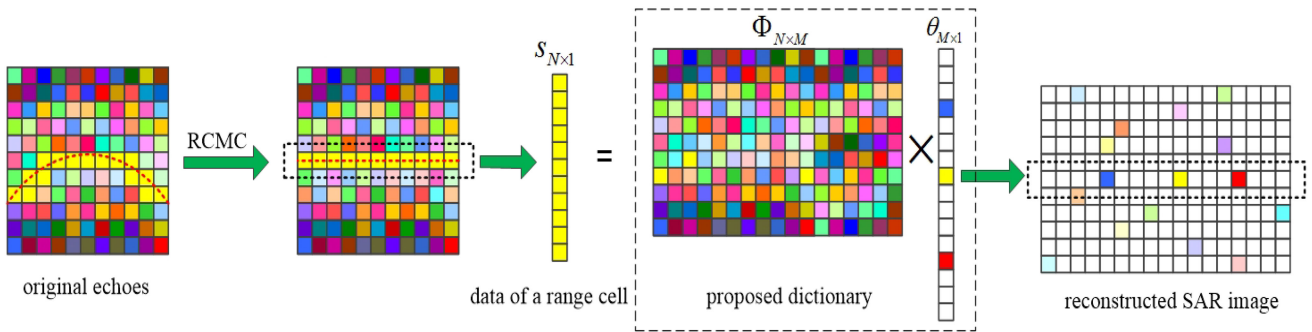
Fig. 1. CS-based moving target imaging.

In this article, a novel CS-based moving target imaging mode is proposed for HRWS SAR based on multiple receive apertures in azimuth for the first time. The proposed algorithm is mainly divided into two parts: MC-SAR echo signal processing and CS-based imaging. Prior to CS-based imaging, SAR echo signal processing primarily performs azimuth signal reconstruction and multichannel RCM correction (RCMC) [24]–[26] to improve azimuth resolution for imaging. However, due to the velocity of moving targets, the reconstructed echo is equivalent to being modulated by the signal with periodic phase error [2], [27] when the method of multichannel uniformly displaced phase center sampling [28] is used for signal reconstruction. Such phase error is linearly dependent on range frequency and is known as frequency-dependent phase mismatch (FD-PM). The periodicity of the FD-PM increases the difficulty of RCMC, which is also a challenge for subsequent CS imaging. Specifically, RCMC algorithm for MC-SAR system is designed when the sampling frequency is lower than the Nyquist rate. Furthermore, a novel dictionary is constructed for CS-based moving target imaging by analyzing the FD-PM. As a result, SAR images with higher azimuth resolution can be acquired with a small amount of data. Finally, simulated experiments are carried out to verify the performance of the proposed CS-based moving target imaging algorithm for MC HRWS SAR.

In summary, the main contributions of this article are twofolded.

1) An improved RCMC is designed for MC-SAR system to eliminate the impact of low sampling rate and FD-PM.
2) A dictionary is built for CS-based MC-SAR imaging by analyzing FD-PM, by which the amount of data in MC-SAR can be greatly reduced.

The rest of this article is organized as follows. Section II briefly introduces the MC-SAR signal model and FD-PM with multichannel signal reconstruction. Section III analyzes the CS-based moving target imaging algorithm in detail, including HRWS SAR RCMC at low sampling rate and the construction method of dictionary matrix. Section IV conducts the simulation experiments to verify the effectiveness of the proposed algorithm. Conclusions are drawn in Section V.

II. FD-PM IN AZIMUTH SIGNAL RECONSTRUCTION

Fig. 1 illustrates the proposed CS-based moving target imaging in MC HRWS SAR system. The RCMC is first applied to the echoes of moving target, by which the defocus problem can be suppressed for the long synthetic aperture time of the MC-SAR system. Then, the corrected echo signals can be sparsely represented by a predesigned imaging dictionary. In this section, after a brief introduction of the moving target signal model of the MC-SAR system, the FD-PM in azimuth signal reconstruction is analyzed.

A. Signal Model

PRF and swath width are always contradictory in SAR system. To satisfy the requirements of wide swath, PRF must be limited. However, low PRF may cause azimuthal Doppler ambiguity [29]. In HRWS SAR system, this problem is overcame by increasing the number of subapertures in the along-track direction. Multiple channels in the azimuth receive the echoes at the same time, which is equivalent to increasing the sampling frequency, i.e., PRF. Then, displaced phase center antenna (DPCA) technique [30]–[32] is used to suppress the Doppler ambiguity effectively for azimuth signal reconstruction. In fact, the motion of the radar brings signal Doppler broadening. This can easily result in the Doppler of the moving target signal to be submerged in the clutter Doppler, which makes the moving target difficult to be detected. Using DPCA can also eliminate clutter from stationary objects.

Fig. 2 illustrates a two-dimensional MC-SAR moving target imaging model. The direction of the X-axis represents the radar platform speed direction, and the platform moves along the X-axis direction at a speed of v. The target P moves in the Y-axis direction at a speed of v_y and the Y-axis is perpendicular to the X-axis. Since the azimuth velocity of the target does not affect the subsequent RCMC, it is set to 0. Generally, only one channel in a multichannel system transmits wide-beam chirp signals and all channels simultaneously receive scene echo signals. The transmitting channel is considered as the reference channel.

The echoes received by each channel can be considered as being generated by themselves at the equivalent phase center (EPC). Fig. 3 shows the relationship between the radar aperture position and the EPC position. The azimuth distance between two EPC is $d/2$, where d is the actual distance between the apertures.

The reference channel is assumed to be located at $X = 0$ in X-direction when the time $t_m = 0$, where t_m represents the slow time in the azimuth direction when the mth pulse is transmitted.
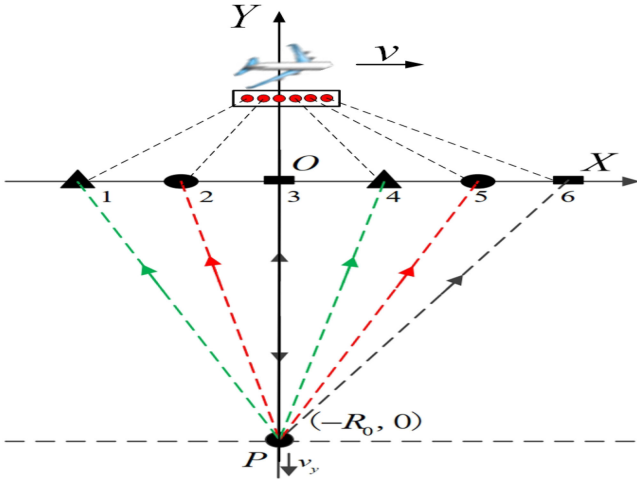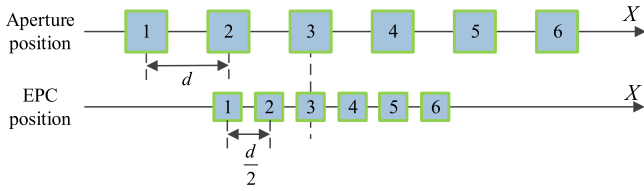
Fig. 2. Multichannel SAR signal model.

Fig. 3. Aperture position and EPC position.

Fig. 4. Illustration of the signal reconstruction process of an MC-SAR system with six channels.

At the moment, the coordinate of the target P is $(-R_0, 0)$, in which R_0 is the nearest range between the platform and the moving target. Let $R_n(t_m)$ represent the instantaneous slant range between the nth channel and the moving target, where $n = 1, 2, \ldots, N_0$, and N_0 is the number of channels. For the side looking SAR, according to the geometry, the second-order Taylor series approximation of $R_n(t_m)$ can be express as

$$
\begin{aligned}
R_n(t_m) &= \sqrt{(v \cdot t_m + d_n)^2 + (R_0 + v_y \cdot t_m)^2} \\
&\approx R_0 + \frac{v^2}{2R_0}(t_m + \Delta t_n - t_c)^2 + v_y(t_m + \Delta t_n - t_c) \\
&\quad - v_y \Delta t_n
\end{aligned}
\tag{1}
$$

where d_n denotes the length of the nth channel from the reference channel, Δt_n is the slow time delay between the nth channel and the reference channel, and $t_c = x_0/v$, in which x_0 represents the X-coordinate of the initial position of the target.

B. Azimuth Signal Reconstruction

In this article, DPCA is adopted to eliminate clutter from stationary objects, and then echoes from different channels are interleaved to reconstruct the azimuth signal. It is known that when using DPCA, the platform speed v, the channel distance d, and PRF need to meet the following conditions:

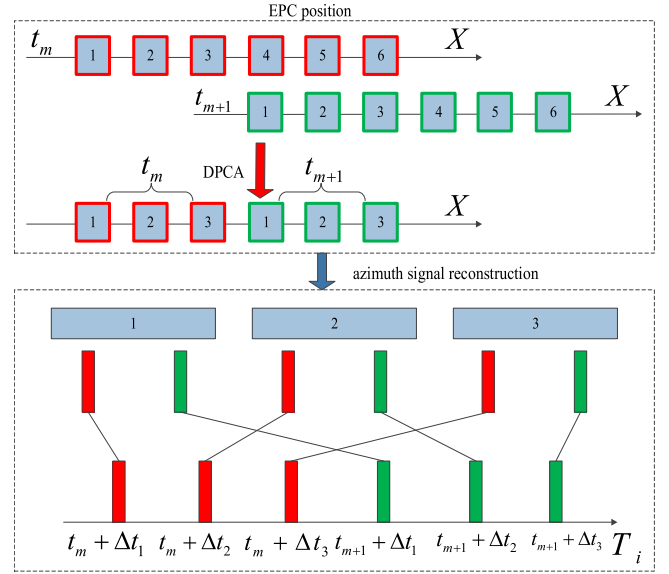$$
\frac{N_1 \cdot d}{2} = \frac{m \cdot v}{\text{PRF}}
\tag{2}
$$

where N_1 is the number of equivalent channels after DPCA and m is a positive integer. In order to ensure uniformly displaced phase center sampling in azimuth, m is set as 1, and thus the following expression can be obtained:

$$
\text{PRF} = \frac{2 \cdot v}{N_1 \cdot d}.
\tag{3}
$$

In order to obtain an SAR image, we need to combine the echo signals of the equivalent channels. In the case of the same PRF of reference channels, the equivalent sampling frequency of N_0 channels is N_1 times that of two channels. When using the space-time equivalent sampling technique for azimuth signal reconstruction, an equivalent azimuth slow time T_i needs to be reconstructed, which can be expressed as

$$
\begin{aligned}
T_i &= t_m + \Delta t_n \\
&= \{\cdots, t_{m-1} + \Delta t_{N_1}, t_m + \Delta t_1 \\
&\qquad \cdots, t_m + \Delta t_{N_1}, t_{m+1} + \Delta t_1, \ldots\} \\
&\quad n = 1, 2, \ldots, N_1, i = (m-1) \cdot N_1 + n
\end{aligned}
\tag{4}
$$

where Δt_n is the delay time between the reference channel and the nth channel along the azimuth slow time. Taking $N_0 = 6$ as an example, the principle of signal reconstruction is illustrated in Fig. 4.

For moving target imaging, at each low time, a linear-frequency-modulated signal is transmitted by the reference channel and received by all channels of the HRWS SAR system. Suppose there are Q distinguishable scattering points in the scene. After range compression, the reconstructed signal is converted into the range-frequency and azimuth-time domains,

which can be expressed as

$$
s(f_r, T_i) = \sum_{q=1}^{Q} \sigma_q w_r(f_r) w_a(T_i) \cdot \exp\left\{ -j\frac{4\pi}{c}(f_c + f_r) \right.
$$
$$
\left. \cdot \left(R_0 + \frac{v^2}{2R_0}\left(T_i - t_c^{(q)}\right)^2 + v_y\left(T_i - t_c^{(q)}\right) \right) \right\}
$$
$$
\cdot \exp\left(j\frac{4\pi}{c}(f_c + f_r) \cdot \Delta\phi_i \right) \tag{5}
$$

where f_c denotes the carrier frequency of the transmitted signal, f_r represents the frequency which is corresponds to the Fourier transform of the range fast time, σ_q is the complex reflection coefficient of the qth scattering point, c is the speed of light, $w_r(f_r)$ represents the range-frequency window function, and $w_a(T_i)$ is the azimuth-time window function.

In (5), $\exp(j\frac{4\pi}{c}(f_c + f_r) \cdot \Delta\phi_i)$ represents an error signal that is periodically modulated due to the radial velocity of moving targets, and the phase error of "$\frac{4\pi}{c}(f_c + f_r) \cdot \Delta\phi_i$" is called FD-PM, in which $\Delta\phi_i$ can be expressed as

$$
\Delta\phi_i = v_y \cdot \Delta t_n
$$
$$
= \{\cdots, v_y\Delta t_{N_1}, v_y\Delta t_1, v_y\Delta t_2, \ldots, v_y\Delta t_{N_1}, v_y\Delta t_1 \cdots\}. \tag{6}
$$

III. MC-SAR MOVING TARGET IMAGING BASED ON CS THEORY

In this section, the specific process of proposed RCMC for multichannel reconstructed signals with unknown motion parameters is presented. In addition, the dictionary construction for CS imaging based on FD-PM is also discussed in detail.

A. RCMC for MC HRWS SAR

Generally, the motion of the radar platform and the long synthetic aperture time can result in a wider Doppler band for the moving target in SAR HRWS system, which is beneficial for improving the azimuth resolution. However, large RCM caused by long synthetic aperture time cannot be neglected in high-precision imaging. Consequently, RCMC should be conducted to remove such RCM. In order to reduce the data volume in the imaging system, in the proposed MC HRWS SAR system, we reduce the sampling rate below Nyquist rate, which means the azimuth-equivalent PRF will be lower than the Doppler bandwidth of the moving target. Moreover, the radial velocity of the moving target will shift the Doppler center frequency even across the baseband. All of these factors will cause the signal Doppler spectrum to alias, resulting in difficulties to RCMC. Moreover, the periodicity of the FD-PM also increases the difficulty of RCMC in an MC-SAR system. Therefore, traditional RCMC algorithm, such as keystone transform [33]–[36] that is usually used for single channel system, cannot be directly applied to the proposed MC systems under a low sampling rate. As a result, an RCMC algorithm is designed for the considered MC-SAR.

According to (5), we can derive that $f_{dc} = 2v_y(f_c + f_r)/c$ is the Doppler centroid. Let the azimuth sampling frequency be F_s, then the sampling aliasing region of the moving target satisfies

$$
F_{\text{band}} = M \cdot F_s + [-F_s/2, F_s/2] \tag{7}
$$

where M is a natural number. In order to well reconstruct echo signals without distortion, the target signal Doppler band should be completely located in just one aliasing region without crossing the adjacent region. Therefore, azimuth deramp [37] processing is first conducted to compress the azimuth spectrum, such that spectrum aliasing caused by low PRF can be avoided. Considering the properties of periodic modulation of reconstructed signal, the equivalent channels are handled separately. Taking the second equivalent reference channel as an example, according to (5), the target signal it receives can be rewritten as

$$
s_2(f_r, t_{m_2}) = \sum_{q=1}^{Q} A \cdot \exp\left\{ j\frac{4\pi}{c}(f_c + f_r) \cdot (v_y \cdot \Delta t_2) \right\}
$$
$$
\cdot \exp\left\{ -j\frac{4\pi}{c}(f_c + f_r) \cdot \left(R_0 \right.\right.
$$
$$
\left.\left. + \frac{v^2}{2R_0}\left(t_{m_2} - t_c^{(q)}\right)^2 + v_y\left(t_{m_2} - t_c^{(q)}\right) \right) \right\} \tag{8}
$$

where $A = \sigma_q w_r(f_r) w_a(t_{m_2})$, t_{m_2} represents the time of the second channel when the time of the reference channel is t_m. It can be easily found that the relationship between t_{m_2} and t_m satisfies

$$
t_{m_2} = t_m + \Delta t_2. \tag{9}
$$

Then, deramp processing is formulated as

$$
H_1 = \exp\left\{ j\frac{4\pi}{c}(f_c + f_r) \cdot \frac{v^2}{2R_0}t_{m_2}^2 \right\}. \tag{10}
$$

By multiplying (10) by (8), we get

$$
s_2(f_r, t_{m_2}) = \sum_{q=1}^{Q} A \cdot \exp\left\{ j\frac{4\pi}{c}(f_c + f_r) \cdot (v_y \cdot \Delta t_2) \right\}
$$
$$
\cdot \exp\left\{ -j\frac{4\pi}{c}(f_c + f_r) \cdot R_{0e}^{(q)} \right\}
$$
$$
\cdot \exp\left\{ -j\frac{4\pi}{c}(f_c + f_r) \cdot v_{ye}^{(q)} \cdot t_{m_2} \right\}. \tag{11}
$$

In which

$$
R_{0e}^{(q)} = R_0 - v_y \cdot t_c^{(q)} + \frac{v^2}{2R_0}t_c^{(q)2} \tag{12a}
$$

$$
v_{ye}^{(q)} = v_y - \frac{v^2}{R_0}t_c^{(q)}. \tag{12b}
$$

In (8), the second index term contains RCM, which is composed of a linear version and a quadratic version. RCM transforms the signal s_2 into a curve in the range-time and azimuth-time domains. According to (11), after deramp processing, the quadratic RCM has been eliminated. Moreover, the azimuth

spectrum of the moving target is significantly compressed, indicating that the probability of the Doppler band spanning the adjacent aliasing region is greatly reduced.

In order to eliminate the Doppler band spanning aliasing region caused by the velocity, a frequency shift function defined by (13) is multiplied to s_2 defined in (11)

$$H_2(f_r, t_{m_2}) = \exp\left(j\frac{4\pi}{c}(f_c + f_r)\frac{\text{PRF} \cdot \lambda}{4}t_{m_2}\right). \quad (13)$$

In order to obtain high-resolution SAR images, the linear RCM must be further removed. In this article, the keystone transform is used to eliminate linear RCM. Actually, keystone transform is a substitution of variables. By defining a new slow-time variable τ_{m_2}, τ_{m_2}, and t_{m_2} own the following relationship:

$$t_{m_2} = \frac{f_c}{f_c + f_r}\tau_{m_2}. \quad (14)$$

Then, the signal can be formulated as

$$s_2(f_r, \tau_{m_2}) = \sum_{q=1}^{Q} A \cdot \exp\left\{j\frac{4\pi}{c}(f_c + f_r) \cdot (v_y \cdot \Delta t_2)\right\}$$
$$\cdot \exp\left\{-j\frac{4\pi}{c}(f_c + f_r) \cdot R_{0e}^{(q)}\right\}$$
$$\cdot \exp\left\{-j\frac{4\pi}{c} \cdot f_c \cdot v_{ye}^{(q)} \cdot \tau_{m_2}\right\}. \quad (15)$$

The support domain of signal data after time transformation is trapezoidal. By interpolating it into a rectangle, we have

$$s_2(f_r, t_{m_2}) = \sum_{q=1}^{Q} A \cdot \exp\left\{j\frac{4\pi}{c}(f_c + f_r) \cdot (v_y \cdot \Delta t_2)\right\}$$
$$\cdot \exp\left\{-j\frac{4\pi}{c}(f_c + f_r) \cdot R_{0e}^{(q)}\right\}$$
$$\cdot \exp\left\{-j\frac{4\pi}{c} \cdot f_c \cdot v_{ye}^{(q)} \cdot t_{m_2}\right\}. \quad (16)$$

By further applying inverse Fourier transform to the signal defined in (16) in the range-frequency domain, the signal of the second channel can be finally transformed into

$$s_2(\hat{t}, t_{m_2}) = \sum_{q=1}^{Q} \tilde{A} \cdot \exp\left\{-j\frac{4\pi}{c} \cdot f_c \cdot v_{ye}^{(q)} \cdot t_m\right\} \quad (17)$$

where $\hat{t}$ represents the range fast time. In (16), terms $\exp\{j\frac{4\pi}{c}(f_c + f_r)\cdot(v_y \cdot \Delta t_2)\}$ and $\exp\{-j\frac{4\pi}{c}(f_c + f_r)\cdot R_{0e}^{(q)}\}$ are independent of time t_{m_2}, so $\tilde{A}$ can be regarded as a constant term. Actually, as shown in Fig. 1, keystone transform makes the envelope of s_2 a straight line in the range-time and azimuth-time domains.

The signals in the other equivalent channels can be processed in the same way as the second equivalent channels. Consequently, the signals of all channels are reconstructed, which can

be expressed as

$$s(\hat{t}, T_i) = \sum_{q=1}^{Q} \tilde{A} \cdot \exp\left\{-j\frac{4\pi}{c} \cdot f_c \cdot v_{ye}^{(q)} \cdot T_i\right\}. \quad (18)$$

It is observed that the radial velocity v_y of the moving target is not used throughout the RCMC. Such RCMC is actually implemented in the case of unknown target motion parameters. In addition, the separate processing of different channels makes the influence of FD-PM negligible. This enables keystone transform to be successfully applied to MC-SAR systems.

B. CS-Based Moving Target Imaging

CS theory indicates that accurate restoration of high-dimensional sparse signals can be achieved by using low-dimensional observation data. For a discrete signal $x \in \mathcal{C}^{M \times 1}$, it can be sparsely represented as following equation when sampling at a higher rate than Nyquist rate:

$$x = \Psi\theta \quad (19)$$

where $\Psi \in \mathcal{C}^{M \times M}$ is a sparse basis and $\theta \in \mathcal{C}^{M \times 1}$ is the sparse representation of x in basis Ψ, which only contains K nonzero elements (without loss of generality, $K < M$). By sampling at a rate much smaller than the Nyquist rate, a sampling signal with length of $N(N < M)$ can be obtained as

$$s = Ax = A\Psi\theta = \Phi\theta \quad (20)$$

where $A \in \mathcal{R}^{N \times M}$ is the measurement matrix of signal x, determining what frequency is used. After downsampling by A, the amount of data will definitely be decreased. Note that in (20), Φ is a dictionary matrix, supporting sparse representation of the single s. Therefore, in order to conduct SAR imaging using CS theory, Φ must be determined in advance.

By analyzing the signal $s(\hat{t}, T_i)$ defined in (18) of a range cell, a dictionary for CS-based SAR imaging can be constructed as follows:

$$\Phi = \left[\varphi\left(\left(-\frac{M}{2} + 1\right) \cdot \Delta t\right), \ldots, \right.$$
$$\left. \varphi(m \cdot \Delta t), \ldots, \varphi\left(\frac{M}{2} \cdot \Delta t\right)\right] \quad (21)$$

where $m = -M/2 + 1, \ldots, M/2$, M is the number of column atoms in the dictionary matrix Φ. The value of Δt is closely related to the azimuth resolution. According to (18), each of the atoms in Φ, i.e., $\varphi(m \cdot \Delta t)$, can be expressed as

$$\varphi(m \cdot \Delta t)$$
$$= \exp\left\{-j\frac{4\pi}{c} \cdot f_c \cdot \left[v_y + \frac{v^2}{R_0} \cdot (m \cdot \Delta t)\right] \cdot T_i\right\}. \quad (22)$$

Considering that $\exp\{-j\frac{4\pi}{c} \cdot f_c \cdot v_y\}$ is constant, $\varphi(m \cdot \Delta t)$ can be simplified as

$$\varphi(m \cdot \Delta t) = \exp\left\{-j\frac{4\pi}{c} \cdot f_c \cdot \frac{v^2}{R_0} \cdot (m \cdot \Delta t) \cdot T_i\right\}. \quad (23)$$

TABLE I
SIMULATION PARAMETERS FOR SINGLE SCATTERING POINT EXPERIMENTS

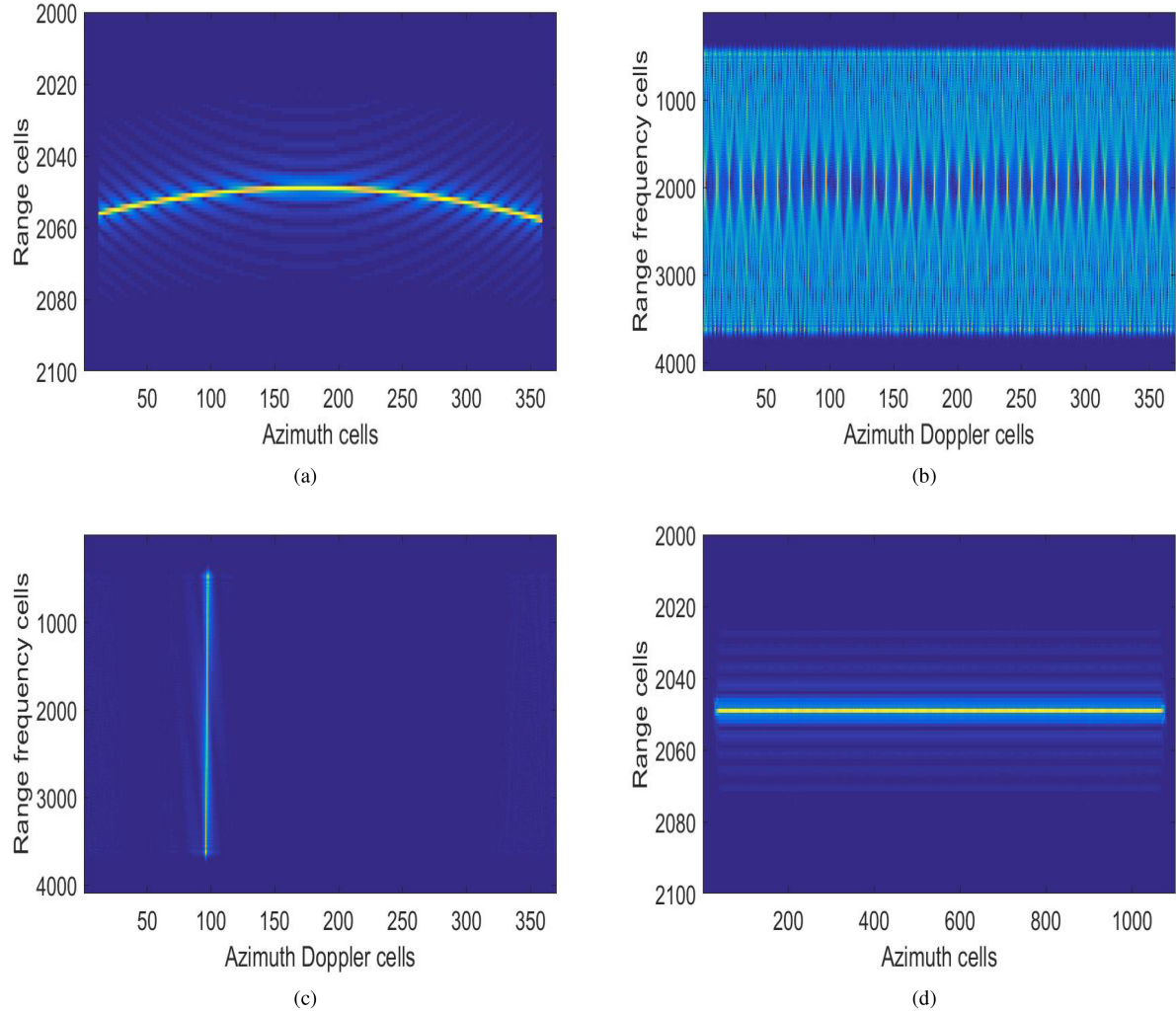| Carrier Frequency	9.7 GHz	Equivalent Channel Number	3
Platform Velocity	500 m/s	Bandwidth of Transmitted Signal	160 MHz
Range Sampling Rate	200 MHz	Nearest Slant Range	7000 m
Pulse Width	10 us	Azimuth Length of Antenna	0.375 m

Fig. 5. Experimental results of RCMC. (a) Echo envelope of the moving target for the reference channel. (b) 2-D frequency spectrum. (c) 2-D frequency spectrum after deramp processing. (d) Multichannel combined signal after keystone transform.

After RCMC for MC HRWS SAR, the effect of FD-PM can be considered negligible. Therefore, there is no need to consider the influence of FD-PM when constructing a dictionary.

Let the signal of a range cell $\boldsymbol{s}(\hat{t}, T_i) = [s(T_1), \ldots, s(T_N)]^{\mathrm{T}}$, $\boldsymbol{\theta} = [\theta_1, \ldots, \theta_M]^{\mathrm{T}}$, where $[\cdot]^{\mathrm{T}}$ denotes transpose of vector or matrix and N is the number of sampling points in the azimuth direction. Then, $\boldsymbol{s}(\hat{t}, T_i)$ can be represented as

$$\boldsymbol{s}_{N \times 1} = \boldsymbol{\Phi}_{N \times M} \boldsymbol{\theta}_{M \times 1} \qquad (24)$$

where $\boldsymbol{\theta}$ is the complex image from the same range cell as $\boldsymbol{s}(\hat{t}, T_i)$. The large value element in $\boldsymbol{\theta}$ corresponds to the scattering points of the moving targets in the imaging scene. In summary, such CS-based moving target imaging process is shown in Fig. 1.

In the dictionary $\boldsymbol{\Phi}$, N represents the number of sampling points in the azimuth direction and M is the number of column atoms. In practice, when PRF remains unchanged, the larger the N, the wider the radar imaging area. However, with the increase of M and N, the speed of solving l_1-based optimization problem will also slow down. The values of M and N depend on the actual number of azimuth samples and Δt in the dictionary. In fact, we will comprehensively consider the values of M and N based on experience, and $N < M$ need to be satisfied.
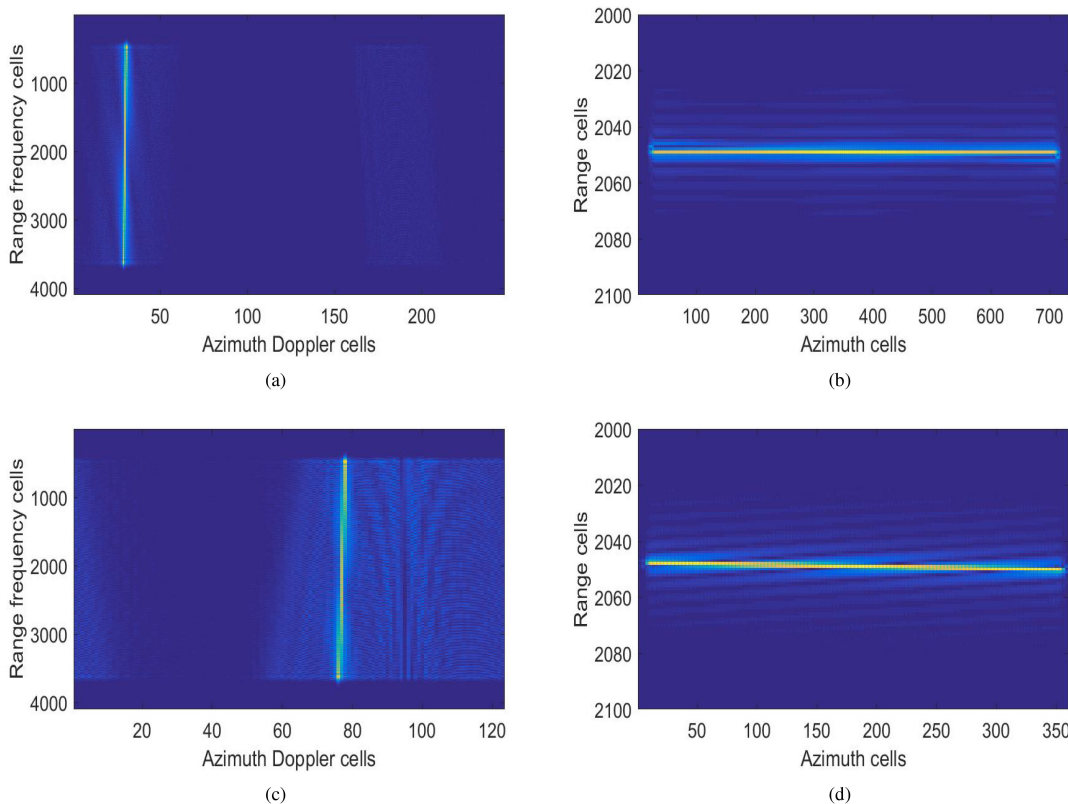
Fig. 6. Experimental results of RCMC after reducing PRF. (a) 2-D frequency spectrum after deramp processing when PRF is 200 Hz. (b) Multichannel combined signal after keystone transform when PRF is 200 Hz. (c) 2-D frequency spectrum after deramp processing when PRF is 100 Hz. (d) Multichannel combined signal after keystone transform when PRF is 100 Hz.
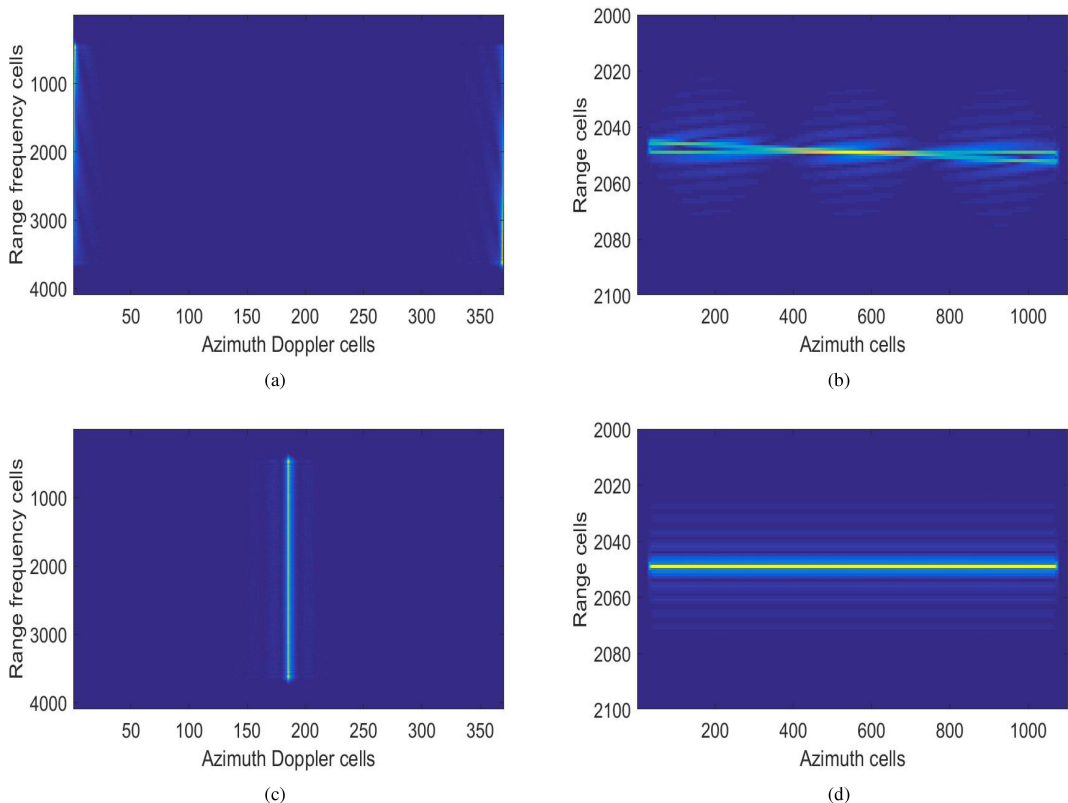

Fig. 7. Experimental results of frequency shift function. (a) 2-D frequency spectrum after deramp processing without using the frequency shift function. (b) Multichannel combined signal after keystone transform without using the frequency shift function. (c) 2-D frequency spectrum after using the frequency shift function. (d) Multichannel combined signal after keystone transform using the frequency shift function.
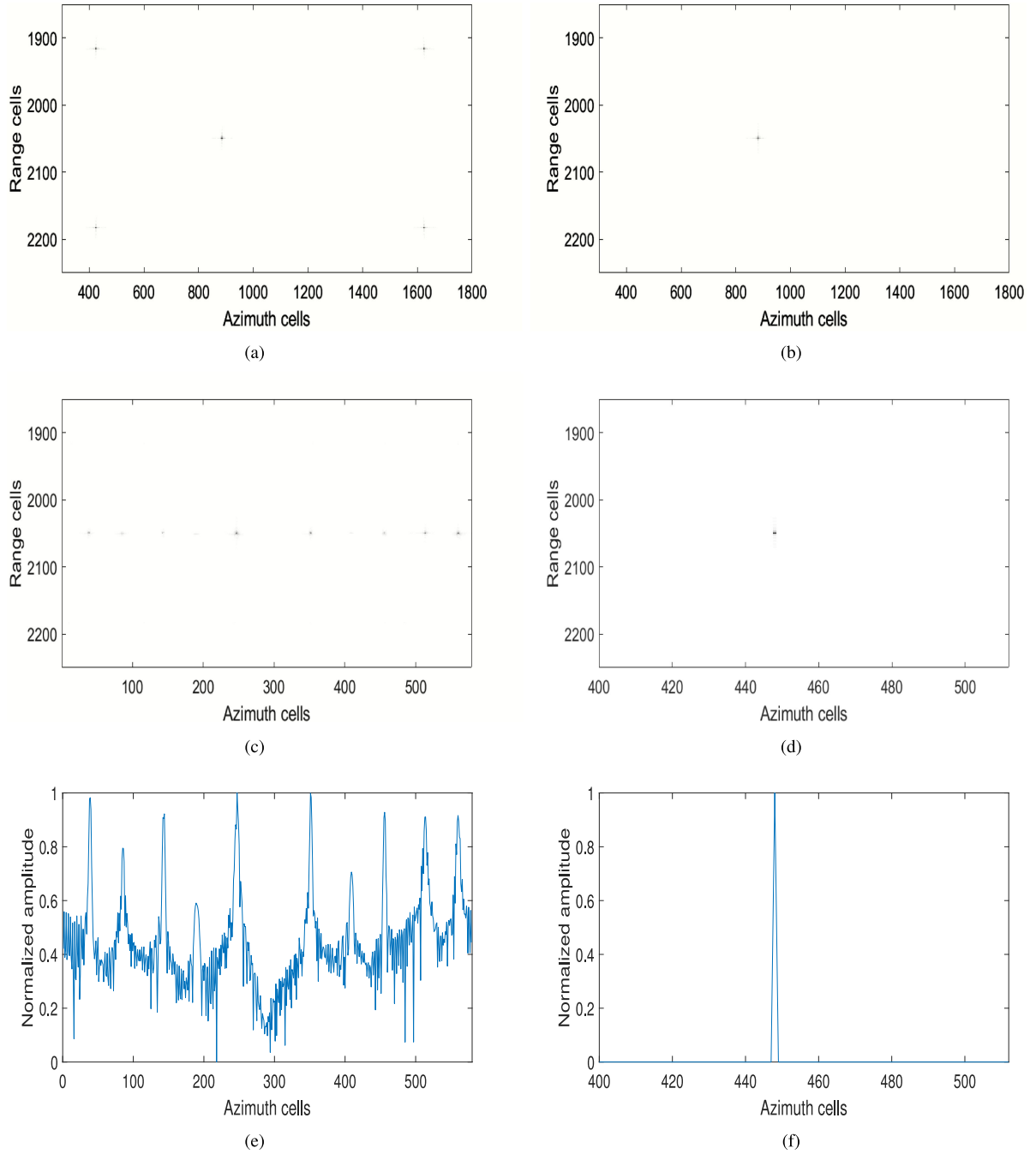
Fig. 8. Experimental results of SAR imaging. (a) Distribution of scattering points in the scene. (b) Six-channel moving target imaging result using RD. (c) Undersampled imaging result using RD. (d) Six-channel moving target imaging result using CS. (e) Cross-sectional view of a certain range cell from (c) using RD. (f) Imaging result of a range cell using CS.

Note that (24) is underdetermined and cannot be easily solved because Φ is a matrix of $N \times M(N < M)$. According to CS theory, the sparse signal θ can be recovered from s through the following optimization problem:

$$\min_{\theta} \|\theta\|_0 \quad \text{s.t.} \quad s = \Phi \cdot \theta \tag{25}$$

where $\| \cdot \|_p$ denotes l_p-norm, and $p = 0, 1, 2, \ldots$. However, the l_0-norm minimization problem defined by (25) is an NP-hard problem. Instead, the l_1-norm minimization is co-solved with the l_0-norm under certain conditions. Therefore, the following l_1-based optimization problem is used for CS-based SAR imaging:

$$\min_{\theta} \|\theta\|_1 \quad \text{s.t.} \quad s = \Phi \cdot \theta. \tag{26}$$

Such optimization problem can be solved using a convex optimization or greedy algorithm [38], [39]. In this article, greedy algorithm orthogonal matched pursuit [39]–[41] is adopted to solve the sparse coefficient due to the high efficiency of it.

IV. EXPERIMENTAL RESULTS AND ANALYSIS

In this section, experiments of a single scattering point, multiple scattering points, and multiple ships for MC-SAR system are conducted, respectively, to verify the effectiveness of the proposed CS-based moving target imaging method.

A. Experiments of a Single Scattering Point

In order to explicitly prove the effectiveness of the RCMC algorithm, experiments of a single scattering point are designed. In these experiments, the six-channel imaging model shown in Fig. 2 is used for validation. Among these six channels, the third channel that transmits wide-beam chirp signals is selected as reference channel. DPCA is applied between channels 1 and 4, 2 and 5, and 3 and 6 to suppress clutter. The number of equivalent channels is $N_1 = 3$. In (4), $\Delta t_1 = -d/v$, $\Delta t_2 = -d/(2v)$, and $\Delta t_3 = 0$. The designed scene consists of four static clutter scattering points and one moving target scattering point. The coordinates of the stationary points are $(-100, 100)$, $(100, 100)$, $(-100, -100)$, and $(100, -100)$, respectively. Since the azimuth velocity of the target does not affect the subsequent RCMC, it is set to 0. When $t_m = 0$, the coordinate of moving target is $(0,0)$. Fig. 8(a) shows the distribution of scattering points in the scene, which is the result of imaging by Range–Doppler (RD) algorithm using the data simulated by a single-channel SAR system whose PRF satisfies the Nyquist rate. Due to the existence of the range velocity of the moving target, the position in the image is azimuthally offset. The simulation parameters for HRWS SAR RCMC experiments are listed in Table I.

It can be calculated from the data in Table I that the Doppler bandwidth of the moving target is 2664.3 Hz. First, the sampling rate is set as 300 Hz, which is far less than the Nyquist rate of 888 Hz. By assuming that the speed of the moving target is 1 m/s, the experimental results of the reference channel, i.e., third channel, are shown in Fig. 5. Because RCM contains both a linear term and a quadratic term, as can be seen from Fig. 5(a), the echo envelope in the range-time and azimuth-time domains is curved. Since the PRF is much smaller than the Nyquist frequency, the two-dimensional spectrum in Fig. 5(b) is heavily aliased and occupies the entire sampling band. After the deramp processing, the quadratic term of the RCM is eliminated. As shown in Fig. 5(c), the azimuth spectrum of the moving target is greatly compressed, completely in the baseband. The echo envelope after multichannel combination is shown in Fig. 5(d). Obviously, the linear component of the RCM is removed using the keystone transform.

It is obvious that RCMC can be effectively implemented when the PRF is greater than 300 Hz. However, the PRF cannot be reduced indefinitely. Therefore, we further set PRF to 200 and 100 Hz, respectively, and the experimental results are shown in Fig. 6. It can be observed that the lower the PRF, the worse the focus of two-dimensional spectrum after deramp processing, and the worse the effect of RCMC. These experimental results show that 300 Hz is the approximate frequency that enables RCMC to be successfully applied while minimizing the amount of data, which is about one-third of the Nyquist rate.
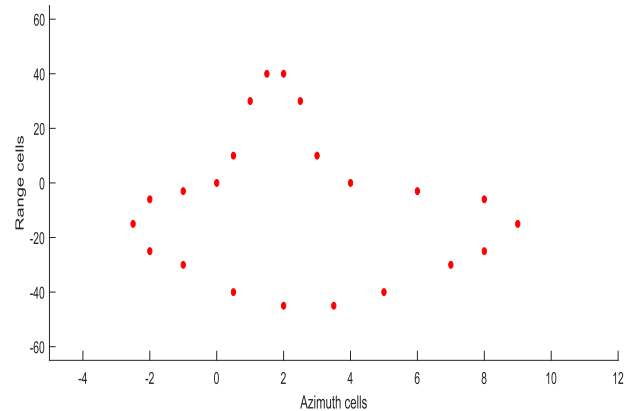

Fig. 9.   Scattering points distribution in the scene.

In order to solve the problem that the two-dimensional spectrum crossing alias band caused by the range velocity of moving target, the frequency shift function defined by (13) is introduced. Fig. 7(a) shows the result of the two-dimensional spectrum shift after azimuth spectrum compression, when the range velocity is 2.21 m/s. Then, the keystone transform is performed without using the frequency shift function, and the result is shown in Fig. 7(b). Obviously, RCMC fails according to Fig. 7(b). After deramp processing, i.e., multiplying (13) to (11), the two-dimensional spectrum is shown in Fig. 7(c). It can be observed that the spectrum can be perfectly preserved in the baseband. Fig. 7(d) further lists the results of the signal envelope in the range-time and azimuth-time domains after using shift function. Compared with Fig. 7(b), the envelopes of the range cells in Fig. 7(d) are parallel to each other, indicating that the RCMC works well.

Next, experiments of CS imaging for HRWS SAR is conducted by applying the proposed dictionary matrix to the results after RCMC in previous experiments. The distribution of scattering points of the simulated scene is shown in Fig. 8(a). Under the condition of Nyquist rate, the scene is imaged by DPCA and RD algorithm using the data simulated by proposed six-channel SAR system, as shown in Fig. 8(b). By reducing the azimuth sampling rate to one-third (300 Hz) of the Nyquist rate, the imaging result by using the RD algorithm is shown in Fig. 8(c). It can be observed that when the amount of sampled data is insufficient, the result of the conventional algorithm is seriously defocused in the azimuth direction and the moving target cannot be detected. When the proposed CS-based algorithm is used at the same frequency, i.e., 300 Hz, the imaging result is shown in Fig. 8(d). It is observed that the clutter scattering point is basically eliminated and the moving target does not defocus. Fig. 8(e) further shows a cross-sectional view of a certain range cell from Fig. 8(c). By reimaging such range cell using the proposed CS-based algorithm, the imaging result is shown in Fig. 8(f). By comparing Fig. 8(e) and Fig. 8(f), there is a sharper peak in Fig. 8(f), indicating that the target image is well focused and not blurred in azimuth. Based on aforementioned analysis, it is obviously that the proposed CS-based imaging algorithm is effective for single scatterer imaging.
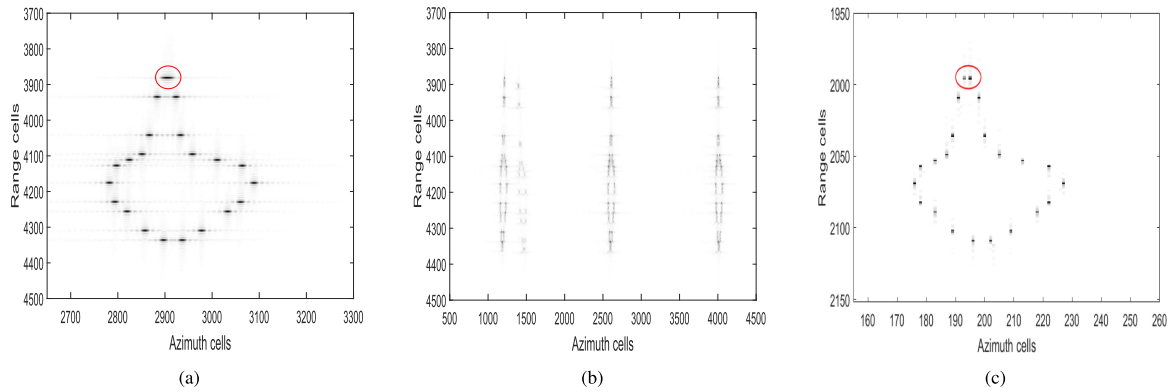
Fig. 10. Imaging results by RD and the proposed CS-based imaging algorithm. (a) Imaging result by RD algorithm at the Nyquist rate. (b) Imaging result by RD algorithm when PRF is 300 Hz. (c) Imaging result by proposed CS-based imaging algorithm when PRF is 300 Hz.

B. Experiments of Multiple Scattering Points

In order to further illustrate the effectiveness of the CS-based imaging method, multiple scattering points experiments are designed. The model and parameters of the MC-SAR system are the same as before. When $t_m = 0$, the scattering points distribution of the scene is shown in Fig. 9, where the stationary clutter points are not shown. At the Nyquist sampling frequency, the imaging result of the scene by RD algorithm is shown in Fig. 10(a). Lowering the sampling frequency, i.e., PRF, to 300 Hz (one-third of the Nyquist rate), the imaging result by RD algorithm is shown in Fig. 10(b). At the same PRF, the imaging result by proposed CS-based imaging algorithm is shown in Fig. 10(c). It can be observed that when the FRF is lower than Nyquist rate, the target image using RD algorithm appears severely blurred and cannot be focused. This problem is greatly alleviated when the PRF increases to Nyquist rate, as shown in Fig. 10(a). However, the two scatterers along the azimuth at the top of the scene cannot be distinguished successfully because they are too close (inside the red circle). Compared with RD algorithm, the proposed CS-based imaging algorithm can separate the two scatterers, as shown in Fig. 10(c). This implies that the azimuth resolution of the proposed algorithm is higher than that of the RD algorithm while the amount of data is greatly reduced.

It should be noted that there is no need to know the speed of each target. The radial velocity of the targets will affect the position of the two-dimensional spectrum after deramp processing and the azimuth position of the targets in the image, but it has almost no effect on the shape of the targets.

In (23), Δt is closely related to the azimuth resolution. The value of Δt is usually about $1/F$, where F is Nyquist rate. In Fig. 10(c), $\Delta t = 1/2200$. In order to illustrate the relation between Δt and azimuth resolution, the experiments of imaging by proposed method with different Δt are conducted. As shown in the first row of Fig. 11, the figures from left to right are imaging results with $\Delta t = 1/800$, $\Delta t = 1/1000$, and $\Delta t = 1/3300$, respectively. As can be seen, when $\Delta t = 1/800$, the two scatterers along the azimuth at the top of the scene cannot be distinguished successfully, and occupy only one pixel (inside the red circle). This indicates that the azimuth resolution is low. In the case

of $\Delta t = 1/1000$, although the two scatterers are separated, occupying two pixels, they are close to each other. However, in Fig. 11(c), the two scatterers are distinguished successfully. This implies that when $\Delta t = 1/3300$, the azimuth resolution is the highest among the above. To illustrate the relation between Δt and azimuth resolution more intuitively, the two scatterers located in another range cell [inside the blue circle in Fig. 10(a)] are analyzed. The second line of Fig. 11 shows the horizontal slices of this range cell imaged by $\Delta t = 1/800$, $\Delta t = 1/1000$, and $\Delta t = 1/3300$ from left to right, respectively. It can be observed that although the positions of the two scatterers in the scene are fixed, the number of azimuth cells between the two scatterers in the image with different Δt is different. When $\Delta t = 1/800$, there are 16 cells between the two scatterers in the image. Lowering Δt to $1/3300$, the distance between the two scatterers in the image is increased to 66 cells, indicating that more potential scatterers can be identified. The aforementioned analysis shows that as Δt decreases, the resolution of the image obtained by proposed method is improved. However, Δt cannot be infinitesimal. In order to obtain an image of the whole scene, the smaller Δt is, the larger M in the proposed dictionary is required. This will greatly increase the time taken to solve optimization problem by using a convex optimization or greedy algorithm.

C. Experiments of Multiple Ships

Fig. 12 shows a real scene of multiple ships imaging by RD algorithm using measured data from a single-channel SAR system, in which radar is side-looking, the PRF is 2000 Hz, the nearest slant range is 12 000 m, and the velocity of airplane is 110 m/s. In order to better prove the effectiveness of our proposed algorithm in practical application, the MC-SAR is also applied to imaging the multiple ships scene shown in Fig. 12. The parameters in Table I are also adopted. In MC-SAR system, the reference channel transmits chirp signals and all channels simultaneously receive scene echoes. After DPCA, the echoes from different channels are interleaved (see Fig. 4) to form the original MC-SAR data. Fig. 13 shows the imaging result of the MC-SAR data using RD algorithm when PRF exceeds Nyquist rate. It is observed that severe defocusing occurs when using RD
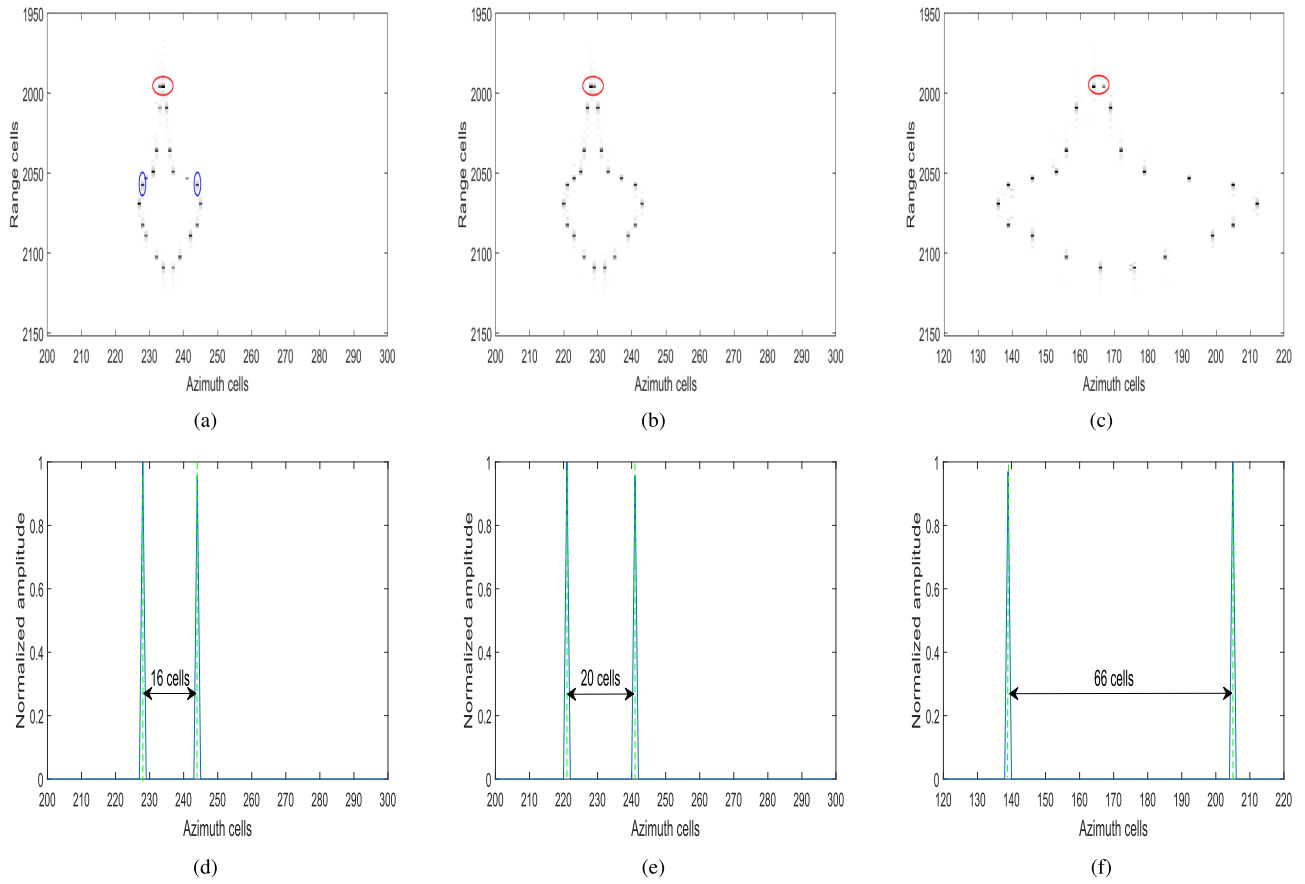
Fig. 11. Imaging results by proposed CS-based imaging algorithm with different Δt. (a) Imaging result when $\Delta t = 1/800$. (b) Imaging result when $\Delta t = 1/1000$. (c) Imaging result when $\Delta t = 1/3300$. (d) Horizontal slices of the two scatterers [inside the blue circle in (a)] imaging by $\Delta t = 1/800$. (e) Horizontal slices of the two scatterers [inside the blue circle in (a)] imaging by $\Delta t = 1/1000$. (f) Horizontal slices of the two scatterers [inside the blue circle in (a)] imaging by $\Delta t = 1/3300$.

Fig. 12. Imaging results of multiple ships by measured single-channel SAR data.
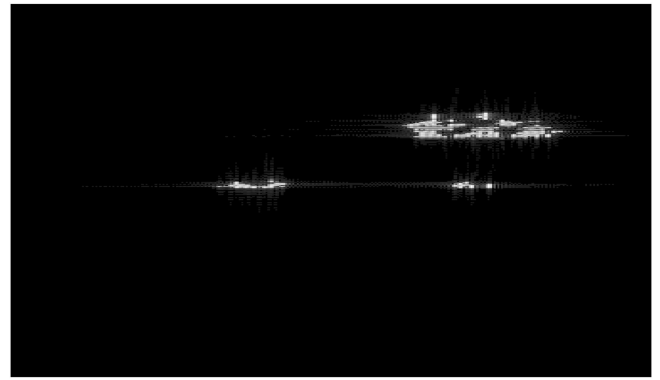

Fig. 13. Imaging results of multiple ships by RD algorithm.

algorithm with PRF exceeding Nyquist rate, though the image is visually similar to that of single-channel SAR shown in Fig. 12. This is because FD-PM has a detrimental effect on RCMC and azimuth compression when using RD algorithm. Unfortunately, such problem cannot be solved by directly removing FD-PM, because the radial velocity of the targets is unknown in practice. When the proposed CS-based imaging algorithm is used, by

reducing PRF to one-third of the Nyquist rate, the original MC-SAR data of the reference channel after range compression are shown in Fig. 14(a). It can be seen that the echo envelope is curved in the range-time and azimuth-time domains, indicating that the RCM cannot be ignored and need to be eliminated. As shown in Fig. 14(b), the two-dimensional spectrum of the signals in Fig. 14(a) is aliased and occupies the entire sampling band due to the low PRF. After deramp processing, as
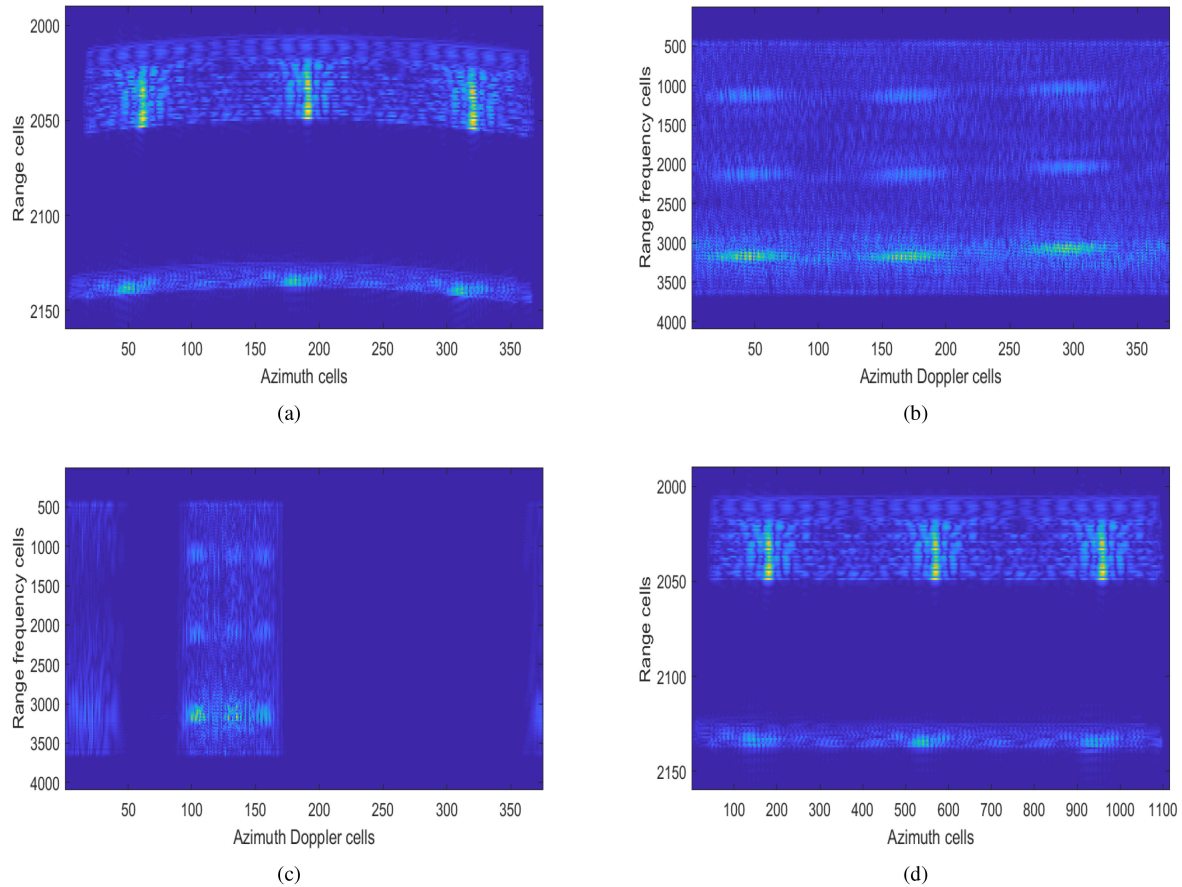
Fig. 14. Experimental results of multiple ships. (a) Echo envelope of multiple ships for the reference channel. (b) 2-D frequency spectrum. (c) 2-D frequency spectrum after deramp processing. (d) Multichannel combined signal after keystone transform.
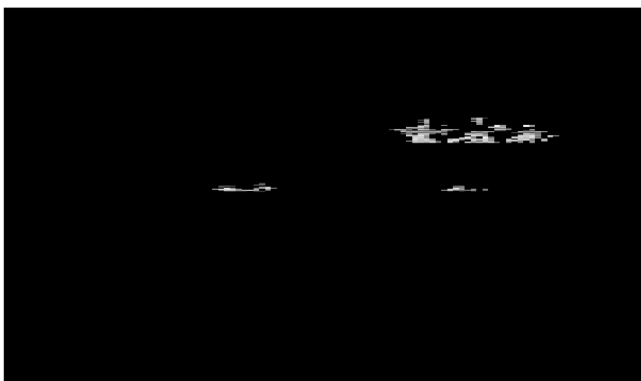

Fig. 15. Imaging results of multiple ships by proposed CS-based imaging algorithm.

shown in Fig. 14(c), the azimuth spectrum is greatly compressed and the signal energy is mainly concentrated in the baseband. By applying keystone transform to the signals after deramp processing, the RCM is completely eliminated, and the result of combining signals from all channels is shown in Fig. 14(d). It can be observed that the echo envelope is horizontal, demonstrating the effectiveness of RCMC. The data after RCMC are used for CS imaging by solving l_1-norm minimization, and the result is

shown in Fig. 15. It can be seen that the proposed CS-based algorithm obviously performs better in azimuth focusing than RD algorithm and the defocusing problem in Fig. 13 can be avoided. This is because l_1-norm minimization makes the side lobe of the reconstructed signal very weak, greatly reducing the influence of the side lobe on the main lobe. In summary, the proposed algorithm can eliminate the adverse effects of FD-PM without directly removing it.

V. CONCLUSION

In this article, a novel moving target imaging CS-based algorithm for the HRWS SAR based on multiple receive apertures in azimuth is proposed. The algorithm performs azimuth sampling at a frequency much lower than the Nyquist rate, realizing multichannel RCMC in the case of unknown target motion parameters. In terms of the dictionary matrix constructed in CS imaging, the algorithm eliminates the effects of FD-PM after filtering out clutter. The results of experiments show that the proposed method obtains image with higher azimuth resolution than traditional method. Furthermore, the reduction in sample rate results in less data, which makes imaging more efficient. Note that the proposed algorithm is suitable for all scenes with sparse targets, in which the considered ocean application is one of typical ones. When targets are not sparse in the scene, the

images generated by the proposed algorithm may appear false targets in the azimuth direction, which desired to be considered in our future work. In addition, it is undeniable that when there is motion error in the platform, the echo data will be mismatched with the dictionary and difficult to image. How to construct a more robust dictionary needs further research.

REFERENCES

[1] S. Zhu, G. Liao, Y. Qu, X. Liu, and Z. Zhou, "A new slant-range velocity ambiguity resolving approach of fast moving targets for SAR system," *IEEE Trans. Geosci. Remote Sens.*, vol. 48, no. 1, pp. 432–451, Jan. 2010.
[2] S. X. Zhang, M. D. Xing, X. G. Xia, R. Guo, and Z. Bao, "A novel moving target imaging algorithm for HRWS SAR based on local maximum-likelihood minimum entropy," *IEEE Trans. Geosci. Remote Sens.*, vol. 52, no. 9, pp. 5333–5348, Sep. 2014.
[3] J. R. Bennett, I. G. Cumming, and R. A. Deane, "The digital processing of Seasat synthetic aperture radar data," in *Proc. IEEE Int. Radar Conf.*, 1980, pp. 168–174.
[4] G. Xu, Y. Gao, J. Li, and M. Xing, "InSAR phase denoising: A review of current technologies and future directions," *IEEE Geosci. Remote Sens. Mag.*, vol. 8, no. 2, pp. 64–82, Jun. 2020.
[5] G. Krieger, N. Gebert, and A. Moreira, "Unambiguous SAR signal reconstruction from nonuniform displaced phase center sampling," *IEEE Geosci. Remote Sens. Lett.*, vol. 1, no. 4, pp. 260–264, Oct. 2004.
[6] N. Gebert, F. Q. de Almeida, and G. Krieger, "Airborne demonstration of multichannel SAR imaging," *IEEE Geosci. Remote Sens. Lett.*, vol. 8, no. 5, pp. 963–967, Sep. 2011.
[7] Z. Li, H. Wang, S. Tao, and B. Zheng, "Generation of wide-swath and high-resolution SAR images from multichannel small spaceborne SAR systems," *IEEE Geosci. Remote Sens. Lett.*, vol. 2, no. 1, pp. 82–86, Jan. 2005.
[8] S. X. Zhang et al., "Multichannel HRWS SAR imaging based on range-variant channel calibration and multi-Doppler-direction restriction ambiguity suppression," *IEEE Trans. Geosci. Remote Sens.*, vol. 52, no. 7, pp. 4306–4327, Jul. 2014.
[9] D. L. Donoho, "Compressed sensing," *IEEE Trans. Inf. Theory*, vol. 52, no. 4, pp. 1289–1306, Apr. 2006.
[10] E. J. Candes, J. Romberg, and T. Tao, "Robust uncertainty principles: Exact signal reconstruction from highly incomplete frequency information," in *IEEE Trans. Inf. Theory*, vol. 52, no. 2, pp. 489–509, Feb. 2006.
[11] E. J. Candes and T. Tao, "Near optimal signal recovery from random projections: Universal encoding strategies?," in *IEEE Trans. Inf. Theory*, vol. 52, no. 12, pp. 5406–5425, Dec. 2006.
[12] M. Ma, S. Mei, S. Wan, J. Hou, Z. Wang, and D. D. Feng, "Video summarization via block sparse dictionary selection," *Neurocomputing*, vol. 378, pp. 197–209, 2020.
[13] L. Zhang et al., "Resolution enhancement for inversed synthetic aperture radar imaging under low SNR via improved compressive sensing," *IEEE Trans. Geosci. Remote Sens.*, vol. 48, no. 10, pp. 3824–3838, Oct. 2010.
[14] W. Weiwei, L. Guisheng, Z. ShengQi, Z. Jie, and Z. Jie, "Compressive sensing-based ground moving target indication for dual-channel synthetic aperture radar," *IET Radar, Sonar, Navigat.*, vol. 7, no. 8, pp. 858–866, 2013.
[15] C. Zhou, F. Liu, Z. Zhu, and B. Li, "A strategy of SAR imaging based on 2-D block compressive sensing," in *Proc. IEEE Int. Conf. Signal Process., Commun. Comput.*, 2013, pp. 1–4.
[16] Y. Liu, Y. Quan, J. Li, L. Zhang, and M. Xing, "SAR imaging of multiple ships based on compressed sensing," in *Proc. 2nd Asian-Pacific Conf. Synthetic Aperture Radar*, 2009, pp. 112–115.
[17] X. C. Xie and L. J. Yu, "A compressive sensing approach for skew-view SAR imaging," in *Proc. IEEE Int. Geosci. Remote Sens. Symp.*, 2016, pp. 5035–5038.
[18] L. Xia, D. Zhu, and J. Rui, "A research on SAR autofocusing algorithms for compressive sensing technique," in *Proc. IET Int. Radar Conf.*, 2013, pp. 1–6.
[19] D. Liu and P. T. Boufounos, "Compressive sensing based 3D SAR imaging with multi-PRF baselines," in *Proc. IEEE Geosci. Remote Sens. Symp.*, 2014, pp. 1301–1304.
[20] A. Budillon, V. Pascazio, and G. Schirinzi, "Compressive sensing methods for SAR imaging," in *Proc. IEEE Int. Geosci. Remote Sens. Symp.*, 2014, pp. 1682–1685.
[21] V. M. Patel, G. Easley, D. Healy, and R. Chellappa, "Compressed synthetic aperture radar," *IEEE J. Sel. Topics Signal Process.*, vol. 4, no. 2, pp. 244–254, Apr. 2010.
[22] H. Mu, Z. Yun, L. Meng, Y. Jiang, and T. Yang, "Detection performance of moving target with compressive sensing via dual-channel spaceborne SAR," in *Proc. IEEE Int. Geosci. Remote Sens. Symp.*, 2016, pp. 1178–1181.
[23] L. Pruente, "Detection performance of GMTI from SAR images with CS," in *Proc. 10th Eur. Conf. Synthetic Aperture Radar*, 2014, pp. 1–4.
[24] S. Zhang, R. Guo, G. Xu, and M. Xing, "Azimuth dependence of quadratic range cell migration correction for the high squint synthetic aperture radar," in *Proc. IEEE CIE Int. Conf. Radar*, 2011, pp. 1502–1505.
[25] C. Dai, X. Zhang, and J. Shi, "Range cell migration correction for bistatic SAR image formation," *IEEE Geosci. Remote Sens. Lett.*, vol. 9, no. 1, pp. 124–128, Jan. 2012.
[26] G. Wang, L. Zhang, and Q. Hu, "A novel range cell migration correction algorithm for highly squinted SAR imaging," in *Proc. Int. Conf. Radar*, 2016, pp. 1–4.
[27] L. Wang, X. Jia, S. Peng, H. F. Kan, and Y. Peng, "Ground moving target indication for MIMO-SAR," in *Proc. Asian-Pacific Conf. Synthetic Aperture Radar*, 2009, pp. 173–176.
[28] L. Lightstone, D. Faubert, and G. Rempel, "Multiple phase centre DPCA for airborne radar," in *Proc. IEEE Nat. Radar Conf.*, 1991, pp. 36–40.
[29] A. Currie and M. A. Brown, "Wide-swath SAR," *IEE Proc. F, Radar Signal Process.*, vol. 139, no. 2, pp. 122–135, 1992.
[30] J. H. Ender, "Detection and estimation of moving target signals by multi-channel SAR," *Int. J. Electron. Commun.*, vol. 50, no. 2, pp. 150–156, 1996.
[31] R. S. Blum, W. L. Melvin, and M. C. Wicks, "An analysis of adaptive DPCA," in *Proc. IEEE Nat. Radar Conf.*, 1996, pp. 303–308.
[32] H. S. C. Wang, "Mainlobe clutter cancellation by DPCA for space-based radars," in *Proc. IEEE Aerospace App. Conf. Digest*, 1991, pp. 1–128.
[33] R. P. Perry, R. C. Dipietro, and R. L. Fante, "SAR imaging of moving targets," *IEEE Trans. Aerosp. Electron. Syst.*, vol. 35, no. 1, pp. 188–200, Jan. 1999.
[34] P. Huang, G. Liao, Z. Yang, X. G. Xia, and J. Ma, "Long-time coherent integration for weak maneuvering target detection and high-order motion parameter estimation based on keystone transform," *IEEE Trans. Signal Process.*, vol. 64, no. 15, pp. 4013–4026, Aug. 2016.
[35] D. Zhu, L. Yong, and Z. Zhu, "A keystone transform without interpolation for SAR ground moving-target imaging," *IEEE Geosci. Remote Sens. Lett.*, vol. 4, no. 1, pp. 18–22, Jan. 2007.
[36] Z. Sun, J. Wu, Z. Li, Y. Huang, and J. Yang, "Highly squint SAR data focusing based on keystone transform and azimuth extended nonlinear chirp scaling," *IEEE Geosci. Remote Sens. Lett.*, vol. 12, no. 1, pp. 145–149, Jan. 2017.
[37] G. Sun, M. Xing, X. G. Xia, Y. Wu, and B. Zheng, "Robust ground moving-target imaging using deramp-keystone processing," *IEEE Trans. Geosci. Remote Sens.*, vol. 51, no. 2, pp. 966–982, Feb. 2013.
[38] T. Blumensath and M. E. Davies, "Gradient pursuits," *IEEE Trans. Signal Process.*, vol. 56, no. 6, pp. 2370–2382, Jun. 2008.
[39] J. A. Tropp and A. C. Gilbert, "Signal recovery from random measurements via orthogonal matching pursuit," *IEEE Trans. Inf. Theory*, vol. 53, no. 12, pp. 4655–4666, Dec. 2007.
[40] S. M. S. Zobly and Y. M. Kadah, "Orthogonal matching pursuit and compressive sampling matching pursuit for Doppler ultrasound signal reconstruction," in *Proc. Cairo Int. Biomed. Eng. Conf.*, 2012, pp. 52–55.
[41] O. Rabaste, L. Savy, and G. Desodt, "Approximate multitarget matched filter for MIMO radar detection via orthogonal matching pursuit," in *Proc. Int. Radar Conf.*, 2014, pp. 1–6.

Shaojie Li was born in Shanxi, China, in 1994. He received the B.S. degree in communication engineering from Xi'an Technological University, Xi'an, China, in 2016. He is currently working toward the Ph.D. degree in information and communication engineering with the School of Electronics and Information, Northwestern Polytechnical University, Xi'an, China.

His major research interest includes SAR imaging.

Shaohui Mei (Senior Member, IEEE) received the B.S. degree in electronics and information engineering and the Ph.D. degree in signal and information processing from the Northwestern Polytechnical University, Xi'an, China, in 2005 and 2011, respectively.

He is currently an Associated Professor with the School of Electronics and Information, Northwestern Polytechnical University. He was a Visiting Student with the University of Sydney, from October 2007 to October 2008. His research interests include hyperspectral remote sensing image processing and applications, intelligent signal and information acquisition and processing, video processing, and SAR imaging.

Dr. Mei was the recipient of Excellent Doctoral Dissertation Award of Shaanxi Province, in 2014 and Best Paper Award of IEEE ISPACS 2017. He is currently serving as the Reviewer of more than 20 international famous academic journals, and was awarded the Best Reviewer of IEEE JOURNAL OF SELECTED TOPICS IN APPLIED EARTH OBSERVATIONS AND REMOTE SENSING, in 2019. He served as the Registration Chair of the IEEE China Summit and International Conference on Signal and Information Processing 2014.

Shuangxi Zhang (Member, IEEE) was born in Fujian, China, 1984. He received the B.S. degree in technique of measuring control and instrument engineering from Xidian University, Xi'an, China, in 2008, and the Ph.D. degree in signal processing from the National Key Laboratory of Radar Signal Processing, Xidian University, in 2014.

He was a Research Fellow with the National University of Singapore during 2014–2016. He is currently an Associate Professor with the School of Electronics and information, Northwestern Polytechnical University, Xi'an, China. His research interests include SAR imaging, SAR interference suppression, array signal processing, electromagnetic scattering, etc.

Dr. Zhang is the Organizer and Session Chairs of Synthetic Aperture Radar Techniques and Applications-Part1/2 and -Part2/2 in ACES-China 2017, Suzhou, China.

Shuai Wan (Member, IEEE) received the B.E. degree in telecommunication engineering and the M.E. degree in communication and information system from Xidian University, Xi'an, China, in 2001 and 2004, respectively, and the Ph.D. degree in electronics engineering from Queen Mary University of London, London, U.K., in 2007.

She is currently a Professor with Northwestern Polytechnical University, Xi'an, China, and an Adjunct Professor with RMIT University, Melbourne, VIC, Australia. Her research interests include versatile video coding, point cloud compression, video processing and streaming, and hyperspectral image processing.

Tao Jia received the B.S. degree in avionics maintenance from Air Force Engineering University, Xi.an, China, in 1999, and the M.S. degree in communications and information systems from Huazhong University of Science and Technology, Wuhan, China, in 2011.

He is currently an Associate Professor with the Air Force Engineering University, Xinyang, China. He has authored/coauthored more than 50 journal papers and four textbooks. His research interests include airborne avionics system and electromagnetic spectrum detection and perception.